Parametric instabilities of interacting bosons in periodically-driven 1D optical lattices

J. Näger[1,2,*], K. Wintersperger[1,2,*], M. Bukov[3,4,*], S. Lellouch[5,6], E. Demler[7], U. Schneider[1,2,8], I. Bloch[1,2], N. Goldman[5], M. Aidelsburger[1,2]

[1] *Fakultät für Physik, Ludwig-Maximilians-Universität München, Schellingstraße 4, 80799 München, Germany*
[2] *Max-Planck-Institut für Quantenoptik, Hans-Kopfermann-Straße 1, 85748 Garching, Germany*
[3] *Department of Physics, Boston University, 590 Commonwealth Avenue, Boston, MA 02215, USA*
[4] *Department of Physics, University of California, Berkeley, CA 94720, USA*
[5] *Center for Nonlinear Phenomena and Complex Systems, Université Libre de Bruxelles, CP 231, Campus Plaine, 1050 Brussels, Belgium*
[6] *Laboratoire de Physique des Lasers, Atomes et Molécules, Université Lille 1 Sciences et Technologies, CNRS, 59655 Villeneuve d'Ascq Cedex, France*
[7] *Department of Physics, Harvard University, Cambridge, MA 02138, USA*
[8] *Cavendish Laboratory, University of Cambridge, J. J. Thomson Avenue, Cambridge CB3 0HE, UK*
[*] *these authors contributed equally to this work*

Periodically-driven quantum systems are currently explored in view of realizing interacting topological phases. This Floquet-engineering approach is particularly promising in gases of ultracold atoms, where topological band structures can be engineered through well-designed shaking protocols, and where inter-particle interactions can be finely tuned. While both features have been demonstrated individually, the interplay between interactions and time-periodic driving can lead to uncontrollable heating and instabilities, potentially preventing any practical application of this scheme. In this work, we experimentally identify the existence of parametric instabilities, which trigger the destruction of weakly-interacting Bose-Einstein condensates in strongly-driven optical lattices through the exponential growth of collective excitations. By monitoring the time evolution of the momentum distribution, we determine the nature of these excitations and demonstrate the crucial role played by the transverse degrees of freedom and the harmonic trap along the lattice axis. We identify the most unstable collective mode, which is shown to dominate the instability, as predicted by Bogoliubov theory. Understanding the onset of instability in driven quantum systems is crucial for determining optimal conditions for realizing strongly-correlated topological states of matter.

Floquet engineering has proven to be a powerful technique for the design of novel quantum systems with tailored properties, otherwise unattainable in conventional static systems [1–5]. It is based on the careful design of time-periodic systems, whose stroboscopic evolution is governed by an effective time-independent Hamiltonian featuring the desired properties. Floquet engineering is captivating due to its conceptual simplicity and its potentially far-reaching applications. Current theoretical efforts include the realization of exotic quantum phases of matter, such as Floquet Chern insulators, by irradiating solid-state systems with light [6–14]. First experimental realizations of Floquet states in topological insulators were recently reported in Refs. [15, 16]. In engineered quantum systems, Floquet-engineering enabled the realization of artificial magnetism and topological Bloch bands in cold atoms [17–26], photonic systems [27–30] and superconducting circuits [31]. These achievements constitute an important step towards a well-controlled realization of interacting topological many-body states, such as fractional Chern insulators [32].

The complex interplay between periodic driving and interactions poses several theoretical and experimental challenges. In time-periodic systems, energy conservation is relaxed due to the absorption and emission of energy quanta from the drive, and any ergodic system is expected to eventually heat up to infinite temperatures [34, 35]. Even though the underlying timescales have been proven to be exponentially long in some cases [36, 37], no rigorous results have been obtained for generic systems, highlighting the importance of developing a conceptual and intuitive understanding of relevant heating processes. Recent experiments [38–42] have addressed this problem for interacting cold-atoms in shaken optical lattices (Fig. 1a). In particular it has been shown theoretically [8, 43, 44] and experimentally [40] that heating rates are well captured by a Floquet Fermi's Golden Rule (FFGR) approach, if they are evaluated at sufficiently long times. This suggests that the long-time dynamics is dominated by incoherent two-body scattering processes [43]. In contrast, the onset of heating is expected to be driven by coherent processes, where the rapid growth of collective excitations in interacting bosonic systems leads to a violent depletion of the Bose-Einstein condensate (BEC) [45–49].

Here, we directly reveal the origin of detrimental heating processes that occur in driven weakly-interacting bosonic lattice systems in certain parameter regimes. These processes are attributed to parametric instabilities caused by the drive that lead to an exponential growth of collective excitations [45, 48]. We theoretically and experimentally study the momentum and instability rate

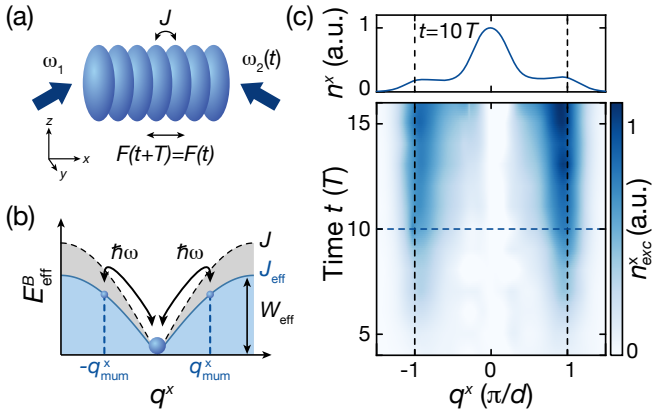

Figure 1. (a) Schematic of the driven 1D optical lattice with tunneling J, generated by two laser beams with frequencies $\omega_{1,2}$, and weak harmonic confinement. Modulating $\omega_2(t)$ periodically with frequency ω generates a force $F(t)$ with period $T = 2\pi/\omega$. (b) Illustration of the effective 1D Bogoliubov dispersion $E^B_{\rm eff}(q^x, J_{\rm eff})$, with width $W_{\rm eff}$ reduced according to the Floquet-renormalized tunnel coupling $J_{\rm eff}$ (blue) compared to the static lattice case (gray). Parametric resonances at $E^B_{\rm eff} = \hbar\omega$ induced by the modulation lead to instabilities centered around the most unstable mode $q^x_{\rm mum}$; $\hbar = h/(2\pi)$ is the reduced Planck's constant. (c) Upper panel: Integrated momentum distribution of the atoms n^x in the first Brillouin zone (BZ), obtained after bandmapping and 6 ms time-of-flight, measured at $t = 10\,T$, for the driving parameters $\alpha_1 = 1.44$ and $\omega/(2\pi) = 800$ Hz. Lower panel: Momentum distribution of the collective excitations $n^x_{\rm exc}$ for the same driving parameters obtained by subtracting the scaled momentum distribution of the BEC at $t = 0$ from the distributions n^x measured at integer multiples of the driving period T, see [33] for details. Each distribution is the average of $\sim$10 individual measurements, which were previously convoluted with a Gaussian of standard deviation $0.04\,\pi/d$. For better visualization, the profiles are further interpolated linearly as a function of time.

of the most unstable mode ("mum"), whose growth dominates the BEC depletion, and compare those measurements to Bogoliubov-theory predictions [45, 48]. According to the latter, parametric instabilities exist whenever the energy quantum $\hbar\omega$ associated with the drive matches the energy of a collective excitation, as dictated by the effective Bogoliubov dispersion $E^B_{\rm eff}(\mathbf{q}, J_{\rm eff})$, where $\mathbf{q}$ denotes the momentum of the excitation and $J_{\rm eff}$ is the effective tunnel coupling renormalized by the drive [50] (Fig. 1b). In a strictly one-dimensional (1D) lattice system, the largest instability occurs on the two-photon resonance, $\hbar\omega = E^B_{\rm eff}(q_{\rm res}, J_{\rm eff})$, which also sets the momentum $q_{\rm mum} = q_{\rm res}$ of the most unstable mode [51]. Consequently, there exists a stable parameter regime for driving frequencies larger than the bandwidth of the effective Bogoliubov dispersion $W_{\rm eff}$. The exact position of the stability boundary is shifted to larger values due to the finite width of the resonance. In the 3D case with weak harmonic confinement transverse to the lattice axis (Fig. 1a), in contrast, parametric instabilities occur via the closely-spaced transverse modes, hindering the existence of a stable parameter regime [40, 44, 45, 48, 52]. Interestingly, we find evidence for a clear separation between lattice and transverse degrees of freedom. Moreover, we reveal a second detrimental effect, which is caused by the presence of an additional harmonic confinement along the lattice axis. Using numerical simulations we show that this leads to parametric instabilities even in the naively expected stable region of a strictly 1D system, where $\hbar\omega > W_{\rm eff}$ and transverse degrees of freedom are frozen.

The appearance of instabilities is common in static weakly-interacting bosonic lattice systems. For instance, dynamical instabilities occur whenever the condensate is prepared at a finite quasimomentum, where the effective mass associated with the band structure is negative [53–58]. We emphasize that the origin of such instabilities is different compared to those revealed in this work, where the BEC is initially in the minimum of the effective band dispersion at $\mathbf{q}=0$ (Fig. 1c) and where parametric instabilities originate from the time-dependent nature of the drive. Finally, we note that a different form of instability, which leads to the collective emission of matter-wave jets, was recently reported in Bose gases subjected to weak time-modulated interactions [59–61].

EXPERIMENTAL SETUP

The experiment starts by loading an almost pure BEC of about $N = 3.7(4) \times 10^5$ ^{39}K atoms within 100 ms into a 1D optical lattice with lattice constant $d = 425$ nm and depth $V_{\rm lat} = 11.0(3)\,{\rm E_R}$, where ${\rm E_R} = h^2/(8md^2) = h \times 7.1$ kHz is the recoil energy and m the mass of an atom. Additional confinement is provided by an optical dipole trap. The harmonic trapping frequencies of the combined potential are $\omega_r/(2\pi) = 26(2)$ Hz in the xy-plane and $\omega_z/(2\pi) = 204(3)$ Hz in the vertical direction. The lattice is aligned along the x-axis and is created by interfering two laser beams with $\lambda = 736.8$ nm under an angle of 120°. The position of the lattice is modulated by varying the frequency of one lattice laser beam, $\omega_2(t) = \omega_1 + 2\pi\nu\sin(\omega t + \varphi)$ (Fig. 1). In the reference frame of the lattice, this leads to a time-varying force $F(t) = F_0\cos(\omega t + \varphi)$, with $F_0 = md\nu\omega$ [50]. Neglecting the transverse modes and the harmonic confinement for now, i.e., considering a homogeneous 1D lattice system, the time-dependent tight-binding Hamiltonian describing the dynamics takes the following form

$$\hat{H}(t) = -J\sum_{\langle ij\rangle}(\hat{a}_i^\dagger\hat{a}_j + \hat{a}_j^\dagger\hat{a}_i) + \frac{U}{2}\sum_j \hat{n}_j(\hat{n}_j - 1) + K\cos(\omega t + \varphi)\sum_j j\hat{n}_j, \quad (1)$$

where $\hat{a}_i^\dagger$ and $\hat{a}_i$ are the bosonic creation and annihilation operators on lattice site i, $\hat{n}_i$ is the corresponding number operator, $J/h = 108(7)$ Hz is the tunnel coupling, U is

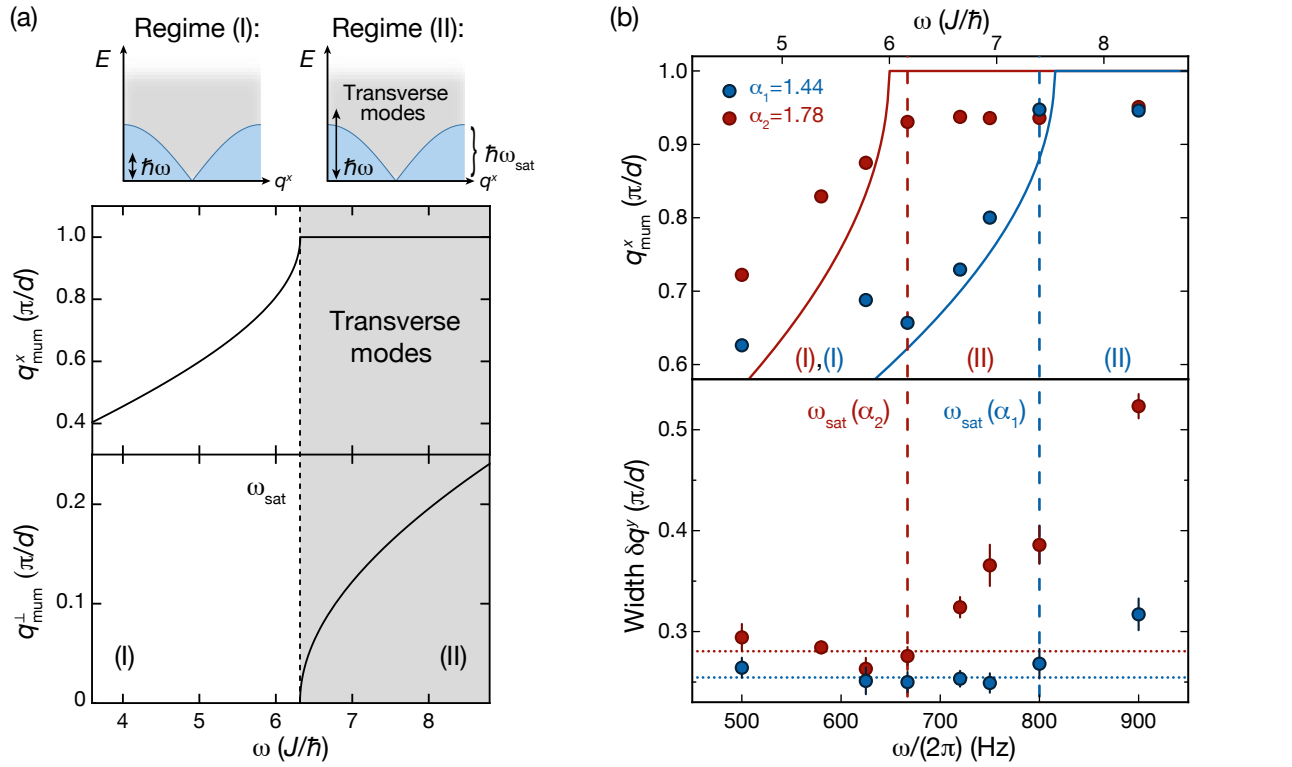

Figure 2. (a) Top: Schematics of the Bogoliubov dispersion in the lattice direction (blue) with finite bandwidth $W_{\rm eff} = \hbar\omega_{\rm sat}$. The gray area illustrates the continuous unbounded spectrum of the transverse degrees of freedom. Bottom: Momentum of the most unstable mode $\mathbf{q}_{\rm mum} = (q^x_{\rm mum}, \mathbf{q}^\perp_{\rm mum})$ as predicted by Bogoliubov theory for $\alpha_1 = 1.44$ and $g = 8.07\,J$, which shows a clear separation between lattice (I) and transverse degrees of freedom (II) at $\omega = \omega_{\rm sat}(\alpha_1) = 6.3\,J/\hbar$. (b) Upper panel: Experimental values of the position of the most unstable mode $q^x_{\rm mum}$ for two modulation amplitudes $\alpha_1 = 1.44$ (blue) and $\alpha_2 = 1.78$ (red) with effective hopping $J_{{\rm eff},1}/h = 59\,{\rm Hz}$ and $J_{{\rm eff},2}/h = 38\,{\rm Hz}$ [33]. The dashed lines are guides to the eye, indicating the transition between the two regimes at $\omega_{\rm sat}(\alpha)$. The solid lines display the analytic result based on Eq. (2) for $g = 12\,J$. Each data point is an average of $\sim$10 independent measurements. The error bars were evaluated based on a bootstrapping approach [33]. Lower panel: Full width of the momentum distribution of the excitations δq^y along the y-axis, which was evaluated at 80% of the peak amplitude [33]. The offset $\delta q^y \approx 0.27\pi/d$ for low frequencies is determined by the width of the condensate and the width of the parametric resonance. The dotted lines are guides to the eye. Each data point is an average of $\sim$10 independent measurements and the error bars display the corresponding standard deviation.

the on-site interaction and $K = F_0 d$. The Feshbach resonance of ^{39}K enables us to work in the weakly-interacting regime at the scattering length $a_s = 20a_0$, with a_0 the Bohr radius, where a mean-field approach is expected to be valid. In the high-frequency limit, $\hbar\omega \gg (J, U)$, Floquet theory predicts that the dynamics should be reasonably well described by a time-independent Bose-Hubbard Hamiltonian [first line of Eq. (1)], with renormalized tunnel coupling $J_{\rm eff} = J\mathcal{J}_0(\alpha)$ [3–5, 50]. Here $\mathcal{J}_\nu$ is the νth-order Bessel function of the first kind and $\alpha = K/(\hbar\omega)$. Note that α is independent of the modulation frequency ω, and that the measurements are performed in a strong-driving regime $1 < \alpha < 2$, where the physical properties are non-perturbative but where the minimum of the effective dispersion remains at $q^x = 0$ [50, 58]. To avoid single-particle resonances [62], the modulation frequency is chosen well below the first single-particle bandgap of the static lattice.

NATURE OF THE MOST UNSTABLE MODE

In order to identify instabilities in the system, we monitor the appearance of collective excitations by measuring the momentum distribution of the atoms as a function of time. We observe a fast growth of excitations at particular momenta after a few driving cycles (Fig. 1c). From these measurements we extract the position $q^x_{\rm mum}$ of the most unstable mode along the lattice axis for different modulation frequencies (Fig. 2b) by evaluating the maxima of the measured momentum distributions n^x_{exc}. We find that $q^x_{\rm mum}(\omega)$ increases with ω until it saturates at $q^x_{\rm mum} \approx \pi/d$, the edge of the Brillouin zone (BZ), at a frequency $\omega_{\rm sat}$ that depends on the drive parameter α. We attribute the observed deviation from π/d to the short time-of-flight used in the experiment [33].

Homogeneous 1D optical lattice

According to the Bogoliubov approach of Refs. [45, 46, 48], this behavior is compatible with parametric instabilities that occur whenever a resonance exists between the two natural energies entering the problem, $\hbar\omega = E^B_{\rm eff}(q^x_{\rm res})$, where the effective Bogoliubov spectrum is given by

$$E^B_{\rm eff}(q^x) = \sqrt{4J_{\rm eff}\sin^2(q^x/2)[4J_{\rm eff}\sin^2(q^x/2)+2g]}. \quad (2)$$

Here, $q^x \in$ BZ is the momentum of an excitation along x and $g = nU$ is the interaction parameter determined by the average particle number on each lattice site. More precisely, the parametric resonance condition selects the most unstable mode $q^x_{\rm res} = q^x_{\rm mum}$, which dominates the instability [48]. The effective dispersion Eq.(2) is bounded and its width $W_{\rm eff} = \sqrt{4J_{\rm eff}[4J_{\rm eff}+2g]}$ depends on both the interaction parameter g and the renormalized tunneling $J_{\rm eff}$. Consequently, the system is expected to be stable for driving frequencies $\omega > \omega_{\rm sat}$, where the saturation frequency $\hbar\omega_{\rm sat} = W_{\rm eff}$ is associated with the width of the effective Bogoliubov dispersion. In particular, the saturation frequency is expected to decrease with increasing α, due to a decreasing bandwidth $W_{\rm eff}$ (Fig. 1b), hence enhancing stability according to the resonance condition [46].

Role of transverse degrees of freedom

In the presence of transverse modes, however, instabilities can occur also in the formerly stable regime of the homogeneous 1D system, i.e., $\omega > \omega_{\rm sat}$. This fundamental change is due to the unbounded nature of the spectrum associated with the weakly-confined transverse directions, as predicted in Ref. [48]. In this case, there is always a set of resonant excitations determined by the resonance condition

$$\hbar\omega = E^B_{\rm eff}(\mathbf{q}_{\rm res}), \quad \mathbf{q}_{\rm res} = (q^x_{\rm res}, \mathbf{q}^\perp_{\rm res}), \quad (3)$$

which causes the system to be necessarily unstable. The most unstable mode is associated with the dominating instability rate $\Gamma = \max_{\mathbf{q}_{\rm res}} \Gamma_{\mathbf{q}_{\rm res}}$. In the previously stable regime ($\omega > \omega_{\rm sat}$) its momentum is obtained by saturating $q^x_{\rm mum} = \pi/d$ and adjusting the transverse component $\mathbf{q}^\perp_{\rm mum}$ according to the resonance condition. This clear separation of the lattice and transverse degrees of freedom is reflected in the two distinct regimes (Fig. 2a):

(I) $\omega < \omega_{\rm sat}$: $\quad q^x_{\rm mum} < \pi/d$ and $|\mathbf{q}^\perp_{\rm mum}| = 0$,

(II) $\omega > \omega_{\rm sat}$: $\quad q^x_{\rm mum} = \pi/d$ and $|\mathbf{q}^\perp_{\rm mum}| > 0$.

In the first regime (I), the modulation mainly couples to excitations along the lattice direction, $q^x_{\rm mum} = 2\arcsin\sqrt{\left(\sqrt{g^2+(\hbar\omega)^2}-g\right)/(4J_{\rm eff})}/d$ and the stability is not affected by the transverse modes ($\mathbf{q}^\perp = 0$). When reaching the second regime (II), the transverse degrees of freedom dominate, $\mathbf{q}^\perp_{\rm mum}$ becomes finite and grows according to $\hbar^2(\mathbf{q}^\perp_{\rm mum})^2/(2m) = \sqrt{g^2+(\hbar\omega)^2} - g - 4J_{\rm eff}$. In the measured momentum distributions, the precise value of the transverse component is masked by the initial momentum spread of the condensate and the width of the parametric resonance. Nevertheless, it manifests itself in a broadening, which we monitor by determining the width δq^y of the condensate along y (Fig. 2b). As expected, we observe that the width $\delta q^y(\omega)$ starts to increase with the frequency for $\omega > \omega_{\rm sat}(\alpha)$, simultaneously with the saturation of $q^x_{\rm mum}$ at the BZ edge. The transition point $\omega_{\rm sat}(\alpha)$ furthermore decreases for larger driving parameters α in line with the reduction of $J_{\rm eff}$ (Fig. 2b). This constitutes the first direct experimental signature of the detrimental role of transverse modes in bosonic systems exploiting Floquet engineering, hence revealing the origin of the heating bottleneck in these systems.

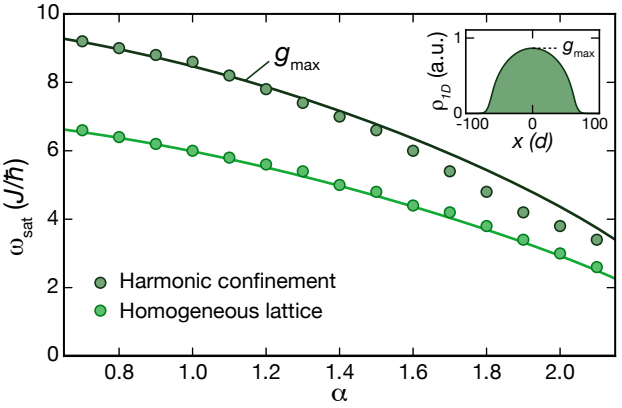

Figure 3. Numerical simulations of the saturation frequency $\omega_{\rm sat}$ for a homogeneous 1D system (light green, $g = 4.29\,J$) and for a harmonically trapped one (dark green, trap frequency $\omega_x = 0.26\,J/\hbar$, $g_{\rm max} = 10.2\,J$). The system size is $L_x = 201\,d$ and the atom number is $N_0 = 1000$. The solid lines are analytic predictions of the saturation frequency at $\hbar\omega_{\rm sat} = W_{\rm eff}$ for a homogeneous 1D lattice with interaction energies g and $g_{\rm max}$ based on Eq. (2). Inset: Initial density distribution $\rho_{1D}(x)$ in the harmonically trapped 1D lattice, which is well described by a Thomas-Fermi profile. It induces a position dependence in the interaction parameter g, where the maximum value $g_{\rm max}$ is determined by the central density.

Harmonic confinement along the lattice

The stability analysis summarized above is based on the bounded nature of the spectrum associated with a homogeneous 1D lattice. In most optical lattice experiments there is, however, an additional harmonic confinement along the lattice axis. As a result, the spectrum is unbounded already along the lattice direction and we do

not expect a truly stable parameter regime to exist even in the absence of transverse modes. In order to understand the dynamics in the presence of a harmonic trap we performed numerical Bogoliubov-de Gennes (BdG) simulations of 1D lattices comparing the position of the most unstable mode with and without harmonic confinement.

Indeed, we find a behavior similar to the homogeneous situation, i.e., the momentum $q^x_{\rm mum}(\omega)$ increases with ω until it saturates at the edge of the BZ at $q^x_{\rm mum} \approx \pi/d$. However, we find a significant shift of the transition frequency $\omega_{\rm sat}$ to larger values, compared to the homogeneous case (Fig. 3). This is caused by the inhomogeneous density distribution of the ground-state wavefunction in the presence of the trap, which effectively increases the interaction parameter in the center of the trap (inset Fig. 3). A larger interaction parameter increases the saturation frequency $\omega_{\rm sat}$, which explains the observed shift [33]. This behavior is reproduced by analytic predictions for a homogeneous lattice evaluated for the maximum interaction parameter $g_{\rm max}$ in the center of the harmonically trapped 1D system (Fig. 3).

The experiment is performed in 3D and from our measured in-situ density profiles we obtain an interaction parameter $g_{\rm max} = 8.1(9)\,J$ in the center of the trap, where the error bar is dominated by atom number fluctuations [33]. The corresponding saturation frequencies predicted by Bogoliubov theory for a homogeneous system evaluated for this interaction parameter are $\omega_{\rm sat}(\alpha_1) = 6.3(3)\,J/\hbar$ (Fig. 2a) and $\omega_{\rm sat}(\alpha_2) = 5.0(3)\,J/\hbar$ respectively. There is a significant shift of about 20 % between the predicted and measured saturation frequencies (Fig. 2b, dashed vertical lines). While this could in principle be explained, for instance, by a systematic error of $\sim 30\%$ in our atom number calibration (Fig. 2b, solid lines), we estimate for realistic parameters that a systematic deviation should not exceed $\gtrsim 20\%$. Moreover, we anticipate that the 1D simulations do not capture all effects introduced by the harmonic trap in a 3D system. Note that the determination of the momentum $q^x_{\rm mum}$ becomes more challenging for smaller driving frequencies, due to the finite width of the condensate, which masks the appearance of the collective excitations [33].

INSTABILITY RATES

Besides the position of the most unstable mode, a characteristic property of parametric instabilities are the associated exponential heating rates Γ, which are dominated by the exponential growth of the occupation of the most unstable mode $n_{q_{\rm mum}}$. In the next sections we present a detailed experimental and numerical study of these rates.

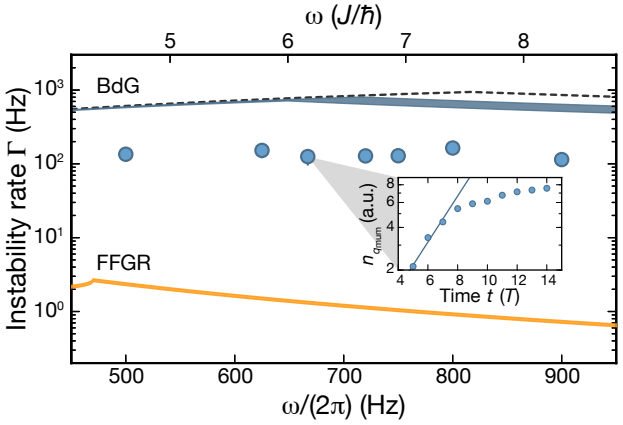

Figure 4. The data points show the instability rates Γ extracted from the measured populations $n_{q_{\rm mum}}$ of the most unstable mode for $\alpha_1 = 1.44$ as displayed in Fig. 2. Each data point is obtained from ~ 10 individual data sets. The error bars are evaluated based on a bootstrapping approach [33] and are generally smaller than the data points. Inset: Measured populations for $\omega/(2\pi) = 667\,$Hz and exponential fit used to extract the instability rate (solid line). The black dashed line shows the result obtained from the BdG equations for $g = 12\,J$ and the blue shaded area the ones obtained for $g = 8.1(9)\,J$ [Eq. (S.14) and (S.16) in [33]], where the width displays the uncertainty in the atom number calibration. Orange shaded area: rates expected from a FFGR approach for the same parameters. Its width is determined by the experimental error in the atom number calibration.

A. Mapping to parametric oscillator

We start with a homogeneous lattice system: A rigorous stability analysis requires a careful treatment of the full time-dependent BdG equations of motion [33, 48], where each collective mode can be formally described in terms of a fictitious parametric oscillator of the form $\ddot{x}(t) + \omega_0^2[1 + A\cos(\omega' t)]x(t) = 0$. Here, A denotes the drive amplitude and ω_0 is the natural frequency of the oscillator. Such oscillators exhibit an instability upon reaching the resonance $\omega' = 2\omega_0$, which is characterized by the rate $\Gamma_{\rm ho} = A\omega_0/4$. In the present context, the mapping between the Bogoliubov equations of motion for each mode $\mathbf{q}$ and the corresponding parametric oscillators is obtained by substituting the driving frequency $\omega' \to 2\omega$, the natural frequency $\omega_0 \to E^B_{\rm eff}(\mathbf{q})/\hbar$ and the amplitude $A \to A_{\mathbf{q}} = 16gJ\mathcal{J}_2(K/(\hbar\omega))\sin^2(q^x/2)/[E^B_{\rm eff}(\mathbf{q})]^2$, where the latter two depend on the excitation momentum $\mathbf{q}$ [33]. The dominating instability rate is evaluated as $\Gamma = \max_{\mathbf{q}_{\rm res}} \Gamma_{\mathbf{q}_{\rm res}}$, with $\Gamma_{\mathbf{q}_{\rm res}} = A_{\mathbf{q}_{\rm res}} E^B_{\rm eff}(\mathbf{q}_{\rm res})/(4\hbar)$, and is shown as a function of the modulation frequency in Fig. 4.

Measured instability rates

Experimentally, we study the instability rates by tracking the occupation of the most unstable mode $n_{q_{\rm mum}}(t)$ as a function of time, as displayed in the inset of Fig. 4. We observe a fast initial increase of the population $n_{q_{\rm mum}}(t)$, which however rapidly slows down for longer times. This deviation from the simple exponential growth predicted by Bogoliubov theory is indeed expected due to non-linear effects inherent to the Gross-Pitaevskii equation (GPE), which are absent in the linearized Bogoliubov analysis. In order to provide a quantitive comparison with theory, we extract the instability rate at short times by restricting the data to the first few modulation periods (inset Fig. 4, [33]). We find that the experimental rates displayed in Fig. 4 are about one order of magnitude lower than the BdG predictions and about two orders of magnitude larger than the FFGR predictions [43], which are expected to describe heating at longer times in terms of incoherent processes [40]. For the timescales probed in the experiment the depletion of the condensate is $\lesssim 10\%$ and we expect atom loss or interactions with thermal atoms to have only negligible influence on the measured rates. Importantly, the discrepancy between the measured rates and the FFGR predictions shows that we are indeed probing the system on sufficiently short timescales, where instabilities are mostly driven by coherent processes, hence enabling us to directly reveal the origin of heating.

Influence of mode coupling: Beyond Bogoliubov

In order to provide more insight on the difference between the experimental instability rates and those predicted by the BdG equations, we performed numerical simulations on a hybrid (translationally-invariant) 2D system [63], composed of one lattice and one continuum direction, based on three different approximation methods [33]: (i) The linearized BdG equations, which capture the parametric instability at short times, i.e., before saturation effects, such as particle-number conservation and non-linear effects associated with the GPE, become significant. (ii) The weak-coupling conserving approximation (WCCA) [47], where particle-number conservation is restored, and which couples the condensate mode to the excitations to leading order in the interaction strength U. This method keeps track of the number of atoms scattered into finite-momentum modes, as well as the back action of the Bogoliubov quasiparticles onto the condensate. The WCCA, however, does not capture collisions between quasiparticles. Hence, it does not offer any insight on the thermalization dynamics at longer times, during which the system heats up steadily to an infinite-temperature state. The BdG and WCCA approaches have already been compared in Ref. [48] and their validity at short times is further confirmed in this work by comparing their predictions to a third approach: (iii) the Truncated Wigner approximation (TWA), which produces thermalizing dynamics and, even though quantum effects are only partially captured in this semi-classical approximation, it has recently been demonstrated that classical Floquet systems thermalize in a very similar way to quantum models [64–66].

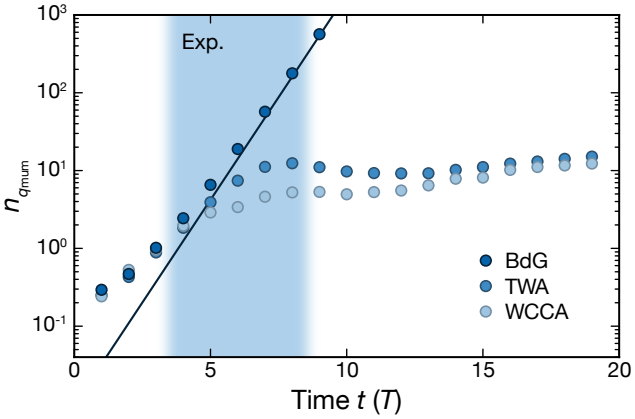

Figure 5. Numerical simulations of the occupation of the most unstable mode $n_{q_{\rm mum}}$ for a homogeneous 2D system (1D lattice and one continuous direction) for $g = 9.52\,J$, $\hbar\omega = 9.25\,J$ and $\alpha_1 = 1.44$ (see [33] for details). The solid line displays the rate obtained from the analytic formulas [Eq. (S.16) in [33]], which is in agreement with the BdG simulations (dark blue) for $t \gtrsim 5T$. The WCCA (blue) and TWA (light blue) partially capture additional non-linear effects and thermalization dynamics, which result in a time-dependent instability rate [33]. Blue shaded area: experimentally accessible time window.

Figure 5 shows the time evolution of the occupation of the most unstable mode. In both, the WCCA and TWA simulations, the obtained curves directly reflect the condensate depletion dynamics. At short times, we find a reasonable agreement between the three theoretical approaches, which further improves as one decreases the on-site interaction strength U, while keeping g fixed. At later times, the three approximations exhibit different behaviors. Due to the lack of particle conservation, the BdG curves grow exponentially in an unphysical and indefinite manner. In contrast, the WCCA and TWA curves show clear manifestations of saturation effects, indicating that the instability rate is a truly time-dependent physical quantity. After an intermediate transient all momentum modes are equally populated, which is expected for an infinite-temperature state that is reached at long times [33]. These results offer a qualitative explanation for the smaller instability rates observed in the experiment, as compared to the rates predicted by the BdG theory, and further highlight the power of the momentum-resolved measurements in revealing parametric instabilities (Fig. 2).

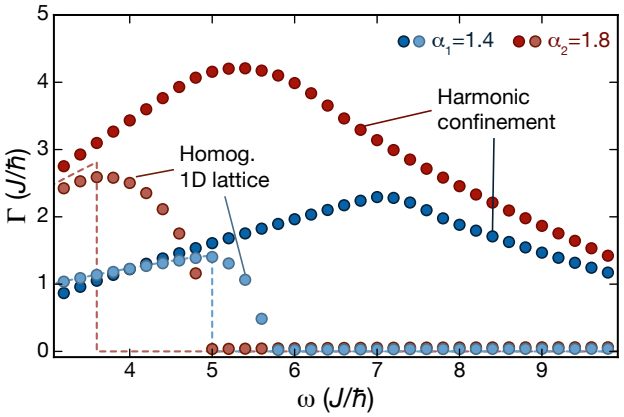

Figure 6. Numerical simulations of the instability rate in homogeneous 1D lattices (light red and light blue, $g = 4.29\,J$) in comparison with the rates in 1D lattices with harmonic confinement (dark red and dark blue, $\omega_x = 0.26\,J/\hbar$ and $g_{\max} = 10.2\,J$) for two different driving parameters $\alpha_1 = 1.4$ (blue) and $\alpha_2 = 1.8$ (red). The system parameters are the same as for the simulations in Fig. 3, i.e., $L_x = 201\,d$ and $N_0 = 1000$. The instability rate was extracted from an exponential fit to the numerical data from the last five out of twenty-four driving cycles of evolution. The dashed lines show the BdG predictions according to Eq. (S.14) in [33] for $g = 4.29\,J$.

DISCUSSION ON STABILITY

Parametric instabilities critically influence the stability of interacting bosonic Floquet systems. We have revealed two detrimental effects that are induced by the presence of transverse modes and a harmonic trap along the lattice direction. While stable parameter regimes are expected to be recovered if the number of transverse modes is suppressed by a tight transverse confinement, the stability in the presence of a harmonic trap along the lattice is a more subtle issue, as we now explain.

In Fig. 6 we show numerically evaluated instability rates of 1D lattice models using BdG simulations. Ideally, a homogeneous 1D system becomes stable for $\omega > \omega_{\rm sat}$. It is known that the stability criterion is shifted to slightly larger values due to the finite width of the parametric resonance [48], as can be seen in our simulations (dashed vertical lines in Fig. 6). In the presence of a harmonic trap, we expect a trivial shift to even larger values, which is determined by the peak interaction parameter $g_{\max}$ of the trapped gas (Fig. 6). Here $\omega_{\rm sat}$ is approximately given by the Bogoliubov bandwidth evaluated for $g_{\max}$ (Fig. 2 and discussion in [33]). For larger modulation frequencies ω, the trapped system displays a distinctly different behavior compared to the homogeneous system. Due to the unbounded nature of the spectrum, there is no true stable parameter regime and the system can always absorb energy via resonant processes. Nonetheless, we find a strong decrease of the instability rates with increasing frequencies, which we attribute to a reduced overlap between the ground and excited state wavefunctions, i.e., localized states at high energies that are known to exist in harmonically trapped lattice systems. As a result, one can recover an approximate stable regime, where the rates are small compared to the duration of the experiment. An alternative way to mitigate this problem in experiments could be provided by the use of uniform box traps [67, 68].

CONCLUSION

We have provided strong evidence that parametric instabilities are responsible for the early-stage depletion of BECs in shaken optical lattices as predicted by Bogoliubov theory. We unveiled the destructive role played by the transverse degrees of freedom and the harmonic confinement along the lattice, which are commonly present in weakly-interacting optical lattice systems. The instability rates observed in the experiment are shown to be overestimated by Bogoliubov theory, which is attributed to a rapid saturation of the collective modes' growth. The latter effect is captured by more involved theories, which take the coupling between Bogoliubov modes and the condensate into account. Our results have strong consequences for future experiments based on Floquet engineering [5], as they indicate the necessity to engineer full-lattice systems where stable regimes can be found [46, 48]. Parametric resonances, as revealed in this work, are expected to be present, whenever the BdG equations of motion include time-periodic features, and hence may turn out to play an important role in a wide family of Floquet-engineered systems, such as periodically-driven superfluids [5] and superconductors [14], photonic devices [69, 70], but also in a cosmological context [71].

We note that complementary signatures of parametric instabilities have been recently investigated with bosonic atoms in periodically-driven 2D optical lattices at JQI [72].

ACKNOWLEDGMENTS

We thank T. Boulier, M. Cheneau, C. Chin, T. Esslinger, L. Fallani, D. Guéry-Odelin, A. Polkovnikov, T. Porto, M. Reitter, L. Tarruell, and D. Sels for insightful discussions. The work in Munich was supported by the Deutsche Forschungsgemeinschaft (FOR2414 Grant No. BL 574/17-1), the European Commission (UQUAM Grant No. 5319278, AQuS), and the Nanosystems Initiative Munich (NIM) Grant No. EXC4. The work in Brussels was financed by the FRS-FNRS (Belgium) and the TopoCold ERC Starting Grant. M. B. acknowledges support from the Emergent Phenomena in Quantum Systems initiative of the Gordon and Betty Moore Foundation. E. D. was supported by Harvard-MIT CUA, NSF Grant No. DMR-1308435, AFOSR Quantum Simulation MURI, AFOSR-MURI Photonic Quantum Matter

(award FA95501610323). We used QuSpin [73, 74] to perform the numerical simulations. The authors are pleased to acknowledge that the computational work reported on in this paper was performed on the Shared Computing Cluster which is administered by Boston University's Research Computing Services.

[1] T. Kitagawa, E. Berg, M. Rudner, and E. Demler, Phys. Rev. B **82**, 235114 (2010).
[2] M. S. Rudner, N. H. Lindner, E. Berg, and M. Levin, Phys. Rev. X **3**, 031005 (2013).
[3] N. Goldman and J. Dalibard, Phys. Rev. X **4**, 031027 (2014).
[4] M. Bukov, L. D'Alessio, and A. Polkovnikov, Adv. Phys. **64**, 139 (2015).
[5] A. Eckardt, Rev. Mod. Phys. **89**, 311 (2017).
[6] T. Oka and H. Aoki, Phys. Rev. B **79**, 081406 (2009).
[7] N. H. Lindner, G. Refael, and V. Galitski, Nat. Phys. **7**, 490 (2011).
[8] T. Kitagawa, T. Oka, A. Brataas, L. Fu, and E. Demler, Phys. Rev. B **84**, 235108 (2011).
[9] D. Fausti, R. I. Tobey, N. Dean, S. Kaiser, A. Dienst, M. C. Hoffmann, S. Pyon, T. Takayama, H. Takagi, and A. Cavalleri, Science **331**, 189 (2011).
[10] J. Cayssol, B. Dóra, F. Simon, and R. Moessner, Phys. Status Solidi RRL **7**, 101 (2013).
[11] A. G. Grushin, Á. Gómez-León, and T. Neupert, Phys. Rev. Lett. **112**, 156801 (2014).
[12] M. Knap, M. Babadi, G. Refael, I. Martin, and E. Demler, Phys. Rev. B **94**, 214504 (2016).
[13] A. Cantaluppi, M. Buzzi, G. Jotzu, D. Nicoletti, M. Mitrano, D. Pontiroli, M. Riccò, A. Perucchi, P. Di Pietro, and A. Cavalleri, arXiv **1705.05939** (2017).
[14] M. Babadi, M. Knap, I. Martin, G. Refael, and E. Demler, Phys. Rev. B **96**, 014512 (2017).
[15] Y. H. Wang, H. Steinberg, P. Jarillo-Herrero, and N. Gedik, Science **342**, 453 (2013).
[16] F. Mahmood, C.-K. Chan, Z. Alpichshev, D. Gardner, Y. Lee, P. A. Lee, and N. Gedik, Nat. Phys. **12**, 306 (2016).
[17] J. Struck, C. Ölschläger, R. Le Targat, P. Soltan-Panahi, A. Eckardt, M. Lewenstein, P. Windpassinger, and K. Sengstock, Science **333**, 996 (2011).
[18] M. Aidelsburger, M. Atala, S. Nascimbène, S. Trotzky, Y. A. Chen, and I. Bloch, Phys. Rev. Lett. **107**, 255301 (2011).
[19] H. Miyake, G. A. Siviloglou, C. J. Kennedy, W. C. Burton, and W. Ketterle, Phys. Rev. Lett. **111**, 185302 (2013).
[20] G. Jotzu, M. Messer, R. Desbuquois, M. Lebrat, T. Uehlinger, D. Greif, and T. Esslinger, Nature **515**, 237 (2014).
[21] M. Aidelsburger, M. Lohse, C. Schweizer, M. Atala, J. T. Barreiro, S. Nascimbène, N. R. Cooper, I. Bloch, and N. Goldman, Nat. Phys. **11**, 162 (2015).
[22] M. Tarnowski, F. N. Ünal, N. Fläschner, B. S. Rem, A. Eckardt, K. Sengstock, and C. Weitenberg, arXiv **1709.01046** (2017).
[23] N. Goldman, G. Juzeliūnas, P. Öhberg, and I. B. Spielman, Rep. Prog. Phys. **77**, 126401 (2014).
[24] J. Dalibard, arXiv **1504.05520** (2015).
[25] N. Goldman, J. C. Budich, and P. Zoller, Nat. Phys. **12**, 639 (2016).
[26] N. R. Cooper, J. Dalibard, and I. B. Spielman, arXiv **1803.00249** (2018).
[27] M. C. Rechtsman, J. M. Zeuner, Y. Plotnik, Y. Lumer, D. Podolsky, F. Dreisow, S. Nolte, M. Segev, and A. Szameit, Nature **496**, 196 (2013).
[28] M. Hafezi, S. Mittal, J. Fan, A. Migdall, and J. M. Taylor, Nat. Photon. **7**, 1001 (2013).
[29] M. Hafezi, Int. J. Mod. Phys. B **28**, 1441002 (2014).
[30] T. Ozawa, H. M. Price, A. Amo, N. Goldman, M. Hafezi, L. Lu, M. Rechtsman, D. Schuster, J. Simon, O. Zilberberg, et al., arXiv **1802.04173** (2018).
[31] P. Roushan, C. Neill, A. Megrant, Y. Chen, R. Babbush, R. Barends, B. Campbell, Z. Chen, B. Chiaro, A. Dunsworth, et al., Nat. Phys. **13**, 146 (2017).
[32] S. A. Parameswaran, R. Roy, and S. L. Sondhi, C. R. Phys. **14**, 816 (2013).
[33] Supplemental Material.
[34] A. Lazarides, A. Das, and R. Moessner, Phys. Rev. Lett. **112**, 150401 (2014).
[35] L. D'Alessio and M. Rigol, Phys. Rev. X **4**, 041048 (2014).
[36] D. A. Abanin, W. De Roeck, and F. Huveneers, Phys. Rev. Lett. **115**, 256803 (2015).
[37] T. Mori, T. Kuwahara, and K. Saito, Phys. Rev. Lett. **116**, 120401 (2016).
[38] G. Jotzu, M. Messer, F. Görg, D. Greif, R. Desbuquois, and T. Esslinger, Phys. Rev. Lett. **115**, 073002 (2015).
[39] C. J. Kennedy, W. C. Burton, W. C. Chung, and W. Ketterle, Nat. Phys. **11**, 859 (2015).
[40] M. Reitter, J. Näger, K. Wintersperger, C. Sträter, I. Bloch, A. Eckardt, and U. Schneider, Phys. Rev. Lett. **119**, 200402 (2017).
[41] C. Cabrera-Gutierrez, E. Michon, M. Arnal, V. Brunaud, T. Kawalec, J. Billy, and D. Guéry-Odelin, arXiv **1808.00345** (2018).
[42] M. Messer, K. Sandholzer, F. Görg, J. Minguzzi, R. Desbuquois, and T. Esslinger, arXiv **1808.00506** (2018).
[43] T. Bilitewski and N. R. Cooper, Phys. Rev. A **91**, 033601 (2015).
[44] T. Bilitewski and N. R. Cooper, Phys. Rev. A **91**, 063611 (2015).
[45] M. Krämer, C. Tozzo, and F. Dalfovo, Phys. Rev. A **71**, 061602 (2005).
[46] C. E. Creffield, Phys. Rev. A **79**, 063612 (2009).
[47] M. Bukov, S. Gopalakrishnan, M. Knap, and E. Demler, Phys. Rev. Lett. **115**, 205301 (2015).
[48] S. Lellouch, M. Bukov, E. Demler, and N. Goldman, Phys. Rev. X **7**, 021015 (2017).
[49] S. Lellouch and N. Goldman, arXiv **1711.08832** (2017).
[50] H. Lignier, C. Sias, D. Ciampini, Y. Singh, A. Zenesini, O. Morsch, and E. Arimondo, Phys. Rev. Lett. **99**, 220403 (2007).
[51] Note that in general there are higher-order corrections to the resonance condition. We performed numerical calculations to confirm that in our parameter regime the simple relation holds within numerical accuracies.

[52] T. Stöferle, H. Moritz, C. Schori, M. Köhl, and T. Esslinger, Phys. Rev. Lett. **92**, 130403 (2004).
[53] B. Wu and Q. Niu, Phys. Rev. A **64**, 061603 (2001).
[54] L. Fallani, L. De Sarlo, J. E. Lye, M. Modugno, R. Saers, C. Fort, and M. Inguscio, Phys. Rev. Lett. **93**, 140406 (2004).
[55] L. De Sarlo, L. Fallani, J. E. Lye, M. Modugno, R. Saers, C. Fort, and M. Inguscio, Phys. Rev. A **72**, 013603 (2005).
[56] N. Gemelke, E. Sarajlic, Y. Bidel, S. Hong, and S. Chu, Phys. Rev. Lett. **95**, 170404 (2005).
[57] G. K. Campbell, J. Mun, M. Boyd, E. W. Streed, W. Ketterle, and D. E. Pritchard, Phys. Rev. Lett. **96**, 020406 (2006).
[58] E. Michon, C. Cabrera-Gutierrez, A. Fortun, M. Berger, M. Arnal, V. Brunaud, J. Billy, C. Petitjean, P. Schlagheck, and D. Guéry-Odelin, arXiv **1707.06092** (2017).
[59] L. W. Clark, A. Gaj, L. Feng, and C. Chin, Nature **551**, 356 (2017).
[60] H. Fu, L. Feng, B. M. Anderson, L. W. Clark, J. Hu, J. W. Andrade, C. Chin, and K. Levin, arXiv **1807.08781** (2018).
[61] Z. Wu and H. Zhai, arXiv **1804.08251** (2018).
[62] M. Weinberg, C. Ölschläger, C. Sträter, S. Prelle, A. Eckardt, K. Sengstock, and J. Simonet, Phys. Rev. A **92**, 043621 (2015).
[63] We expect that the short-time dynamics should be reasonably well captured by a 2D model, as the confining potential is an order of magnitude stronger along the z-axis.
[64] O. Howell, P. Weinberg, D. Sels, A. Polkovnikov, and M. Bukov, arXiv **1802.04910** (2018).
[65] S. Notarnicola, F. Iemini, D. Rossini, R. Fazio, A. Silva, and A. Russomanno, Phys. Rev. E **97**, 022202 (2018).
[66] A. Rajak, R. Citro, and E. G. D. Torre, arXiv **1801.01142** (2018).
[67] L. Corman, L. Chomaz, T. Bienaimé, R. Desbuquois, C. Weitenberg, S. Nascimbène, J. Dalibard, and J. Beugnon, Phys. Rev. Lett. **113**, 135302 (2014).
[68] N. Navon, A. L. Gaunt, R. P. Smith, and Z. Hadzibabic, Science **347**, 167 (2015).
[69] V. Peano, M. Houde, F. Marquardt, and A. A. Clerk, Phys. Rev. X **6**, 041026 (2016).
[70] A. González-Tudela, C. L. Hung, D. E. Chang, J. I. Cirac, and H. J. Kimble, Nat. Photon. **9**, 320 (2015).
[71] J. Berges, K. Boguslavski, S. Schlichting, and R. Venugopalan, Journal of High Energy Physics **2014**, 54 (2014).
[72] Group of T. Porto, talk at DAMOP 2018, Ft. Lauderdale, Florida.
[73] P. Weinberg and M. Bukov, SciPost Phys. **2**, 003 (2017).
[74] P. Weinberg and M. Bukov, arXiv **1804.06782** (2018).

SUPPLEMENTAL MATERIAL

S1. DATA ANALYSIS

A. Determination of the most unstable mode q^x_{mum} and the instability rates Γ

We image the momentum distribution of the cloud after a short time-of-flight (TOF) of 6 ms using high intensity absorption imaging along the z direction, which integrates the distribution along the imaging axis. Then, we select a region-of-interest (ROI) that is large compared to the first Brillouin zone (BZ) and integrate the images along the y direction. Each integrated profile is convoluted with a Gaussian of width $0.04\,\pi/d$ to reduce detection noise. Fluctuations in the imaging beam can lead to an inhomogeneous background which is to first order described by a linear offset in the profiles. We take the 100 outermost pixels on each side of the convoluted profiles and average the x and pixel values to define a linear offset function for each profile which is then subtracted from the profile. Since the position of the atom cloud slightly fluctuates from shot to shot we determine the center of each profile by a Gaussian fit and shift the profile to be centered around $q^x = 0$.

We take ~ 10 independent measurements for each set of parameters and extract the 1D profiles as described above. For each modulation amplitude and frequency we average the 10 profiles at $t = 0$. Then we take each profile at $t > 0$, scale the mean initial profile to the same height and subtract it to obtain the momentum distribution of the satellite peaks n^x_{exc} (Fig. 1c in the main text). In the low depletion limit, where only a small fraction of the total atom number is excited, this scaling only introduces a small error.

To better estimate the error of the position of the most unstable mode q^x_{mum}, we use a bootstrapping method [S1]: From the 10 subtracted profiles for each parameter set at $t > 0$ we randomly choose 10 with replacement, average them and determine the positions of the maxima of the left and right peak in the resulting mean profile. We repeat this process 100 times and then calculate the mean maximum positions and their standard deviation for the left and right peak separately, which we attribute to the most unstable mode $\pm q^x_{\mathrm{mum}}$. The position of the most unstable mode vs. modulation duration is shown as an example in Fig. S1.

For short times $t \lesssim 10\,T$ we observe a constant position of the most unstable mode, however, at later times, additional momentum components start to be populated and the mode with the largest occupation tends to move towards the center of the BZ. This is due to the onset of thermalization via non-linear effects and mode coupling as discussed in the main text.

We define a maximal error of $0.12\,\pi/d$ for q^x_{mum} and discard data sets, where the error is larger than that. This is usually caused by a low signal-to-noise at short times, where the population in the excited mode is still too small. The short-time regime, where q^x_{mum} is constant, is then identified by defining a maximal deviation in the position of consecutive peaks. It is given by the mean deviation between consecutive peaks but restricted to values below $0.05\,\pi/d$. If the deviation increases we conclude that non-linear processes become relevant which marks the end of the short-time regime. All remaining data points for positive and negative quasimomenta are averaged to evaluate the final q^x_{mum}. The results are shown in Fig. 2b in the main text.

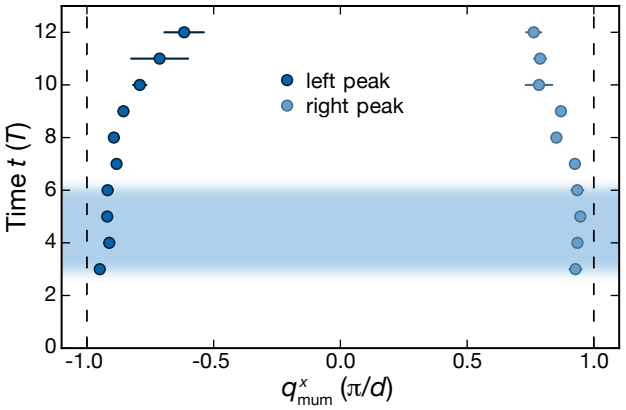

Figure S1. Position of most unstable mode q^x_{mum} as a function of modulation duration t for the negative (dark blue) and positive (light blue) momentum side for $\alpha = 1.78$ and $\omega/(2\pi) = 720$Hz. The shaded region indicates the short time regime for this parameter set as described in the main text that is used in the determination of the properties of the most unstable mode, while the dashed black lines mark the BZ edges.

In the experiment, the momentum of the most unstable mode q^x_{mum} does not fully reach the saturation value π/d. This is explained by a finite TOF, due to which the effects of the insitu size of the cloud on the measured momentum distribution are still significant [S2]. For momenta located at the edge of the BZ, this leads to a significant shift towards the center of the BZ, as seen in Fig. 2b in the main text. We estimate that for the largest momenta a reduction of $\approx 0.1\,\pi/d$ is expected. This estimate is based on a simulated q^x profile after TOF expansion, where we model the insitu distribution with a Gaussian of width $\sigma_0 = 0.1\pi/d$ and the excitations with a Gaussian of width $\sigma = 0.17\pi/d$ centered at $q^x = \pm\pi/d$ and convolve the two. Assuming that the BZ edge imposes a sharp cut on the momentum distribution effectively shifts the center of the distribution towards the BZ center for both the positive and the negative momentum side, while the convolution mainly smoothens the edges of the distribution without having a big influence on the peaks' mean momenta. For momenta that are small compared to the saturation value, the finite TOF has only a minor influence.

In order to extract the instability rates Γ displayed in the inset of Fig. 4 in the main text, we use an exponential

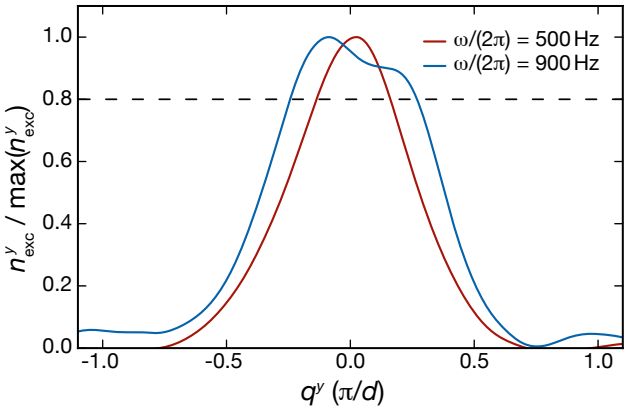

Figure S2. Mean integrated momentum distribution of the atoms perpendicular to the lattice for one driving frequency (500Hz, red) within regime (I) and one driving frequency (900Hz, blue) within regime (II). The dashed black line indicates the evaluation height [see Fig. 2b in the main text].

fit to the observed density at q^x_{mum} for the short time regime idenitfied above.

B. Width of the condensate δq^y

To evaluate the width of the excitation peaks in the y direction, we choose two ROIs that exclude the main condensate, i.e., one ROI for each sign of the respective momentum component of the instability peak. Both ROIs are integrated along the x direction. Again, the resulting profiles are convoluted with a Gaussian of width $0.04\,\pi/d$, shifted so that their mean positions overlap at $q^y = 0$, and then averaged over ~ 10 independent experimental realizations, see Fig. S2. The full width at 80% maximum is evaluated, averaged over all time steps within the short time regime as determined by the evaluation of q^x and finally the satellite peaks at positive and negative momenta are averaged. The result is shown in Fig. 2b in the main text. We evaluate the width at 80% maximum because this is a good trade-off between the large noise at the top produced by a very small slope and high noise at the bottom due to an inhomogeneous background. Also, the relative change in width is bigger at the top of the peak, moving the optimum evaluation height above 50%.

C. Interaction energy

In the experiment we work with a one-dimensional (1D) lattice with harmonic trap confinement along the lattice and in the transverse directions. This results in a 3D inhomogeneous density distribution $\rho(\mathbf{r})$ of the atoms in the lattice and induces a position dependence on the interaction parameter, which is defined as

$$g(\mathbf{r}) = U_0 \rho(\mathbf{r}),$$

with $U_0 = 4\pi\hbar^2 a_s/m$. The density distribution (at $t = 0$) $\rho(\mathbf{r})$ of the atoms is well described by a Thomas-Fermi ansatz:

$$\rho(\mathbf{r}) = \begin{cases} \rho_{\max}\left[1 - \left(\frac{r^2}{R_r^2} + \frac{z^2}{R_z^2}\right)\right] & \text{for } \frac{r^2}{R_r^2} + \frac{z^2}{R_z^2} < 1 \\ 0 & \text{else} \end{cases}$$

Here, the site index l is replaced by the continous position $x = dl$ along the lattice direction such that $\sum_l \frac{1}{d} \to \int \mathrm{d}x$. The peak density is given by

$$\rho_{\max} = \left[\frac{15}{8\pi} N \left(\frac{m\bar{\omega}^3}{2U_0}\right)^{3/2} \zeta\right]^{2/5}.$$

Here, $\bar{\omega} = \sqrt[3]{\omega_r^2 \omega_z}$ is the geometric mean of the measured trapping frequencies with the lattice (see main text) and $\zeta = d \int \mathrm{d}x \, \|w_0(x)\|^4 = 2.08$ with the wannier function of the lowest band $w_0(x)$. Note that this is the effective density that includes the factor ζ that accounts for onsite compression of the atoms, which means the integrated density is $\int \mathrm{d}\mathbf{r} \rho(\mathbf{r}) = N\zeta$. The Thomas-Fermi radii in the presence of the lattice at $a_s = 20 a_0$ are $R_r = 19.8(3)\mu$m and $R_z = 4.0(5)\mu$m.

To determine the atom number, we measure the trapping frequencies in the absence of the lattice ($\tilde{\omega}_r/(2\pi) = 23.2(3)$Hz, $\tilde{\omega}_z/(2\pi) = 189(3)$Hz) and the Thomas-Fermi radii as a function of the scattering length a_s and fit the number of atoms $N = 3.7(4) \cdot 10^5$ according to the Thomas-Fermi prediction. The error represents atom number fluctuations. Note, that for the atom number calibration, the harmonic confinement is reduced compared to the measurements with the lattice that are presented in the main text.

D. Floquet Fermi's Golden Rule

The FFGR rates displayed in Fig. 4 of the main text are computed according to the intra-band heating rates derived in [S3]. The exponential decay of the BEC atoms caused by the modulated lattice can be described as

$$\dot{N}(t) = -\Gamma_{\mathrm{FFGR}} N(t),$$

where $\Gamma_{\mathrm{FFGR}} = \kappa N^{2/5}$. The loss rate κ is independent of the atom number and given by

$$\kappa(\alpha, \omega) = \frac{128}{105} \zeta^{-3/5} \left(\frac{15\pi a_s}{8d}\right)^{7/5} \left(\frac{\hbar\bar{\omega}}{E_R}\right)^{6/5} \frac{E_R}{\hbar} \sum_l \gamma_l$$

with

$$\gamma_l = 6u_l g(s_l)\left(\frac{\zeta J \mathcal{J}_l(\alpha)}{l\hbar\omega}\right)^2$$
$$g(s_l) = \left(\frac{1}{2} - \frac{1}{\pi}\arcsin(1-2s_l)\right) - \frac{2s_l+6}{3\pi}\sqrt{s_l(1-s_l)}$$
$$s_l = \frac{l\hbar\omega}{8J\mathcal{J}_0(\alpha)}$$
$$u_l = \begin{Bmatrix} 0.75 & \text{for} & l \text{ even} \\ 0.15 & \text{for} & l \text{ odd} \end{Bmatrix}$$

and $\mathcal{J}_\nu$ being the ν-th Bessel function of the first kind. For the parameters used here, the rates are dominated by processes up to second order. For the data shown in Fig. 3 in the main text we consider contributions up to $l = 2$.

S2. THEORETICAL METHODS AND ANALYTICAL TREATMENT OF INSTABILITIES IN THE PERIODICALLY-DRIVEN BOSE-HUBBARD MODEL

In this section, we give details about the theoretical methods used to calculate the dynamics and stability properties of the periodically-driven weakly-interacting Bose-Hubbard model (BHM) studied in the main text for a 2D system that consists of one lattice (x-axis) and one continuous direction (y-axis). The latter is defined by the Hamiltonian

$$\begin{aligned}\hat{H}(t) =& -J\sum_{\langle ij\rangle,\mathbf{r}_\perp}(\hat{a}^\dagger_{i,\mathbf{r}_\perp}\hat{a}_{j,\mathbf{r}_\perp} + \text{h.c.}) + \hat{H}_\perp \\ &+ K\cos(\omega t+\varphi)\sum_{j,\mathbf{r}_\perp} j\hat{n}_{j,\mathbf{r}_\perp} \\ &+ \frac{U}{2}\sum_{j,\mathbf{r}_\perp}\hat{n}_{j,\mathbf{r}_\perp}(\hat{n}_{j,\mathbf{r}_\perp}-1). \end{aligned} \tag{S.1}$$

where $\hat{a}_{i,\mathbf{r}_\perp}$ annihilates a particle at lattice site i and transverse position $\mathbf{r}_\perp$. For the implementation of numerical calculations, we discretize the transverse direction according to $\mathbf{r}_\perp = l_\perp d_\perp \hat{\mathbf{e}}_\perp$, where $l_\perp$ labels the fictitious lattice sites along the transverse direction and where $d_\perp$ is set constant [see Sec. S2 F for details]; $J > 0$ denotes the tunneling amplitude of nearest-neighbor hopping along the x direction, $\hat{H}_\perp = \sum_{j,\mathbf{q}^\perp}\frac{(\mathbf{q}^\perp)^2}{2m}\hat{n}_{j,\mathbf{q}^\perp}$ describes a free-particle kinetic part along transverse directions, and $U > 0$ is the repulsive on-site interaction strength. For simplicity we set $\hbar = 1$, the lattice constant $d = 1$ and $d_\perp = 1$ for the whole section. The time-periodic modulation has amplitude K, phase φ, and frequency $\omega = 2\pi/T$ with T the driving period.

Transforming the system to the rotating frame [S4], we eliminate the external shaking at the expense of introducing a periodically-modulated hopping term

$$\begin{aligned}\hat{H}_{\text{rot}}(t) =& -J\sum_{\langle ij\rangle,\mathbf{r}_\perp}(\mathrm{e}^{-i\alpha\sin(\omega t+\varphi)}\hat{a}^\dagger_{i,\mathbf{r}_\perp}\hat{a}_{j,\mathbf{r}_\perp} + \text{h.c.}) \\ &+ \hat{H}_\perp + \frac{U}{2}\sum_{j,\mathbf{r}_\perp}\hat{n}_{j,\mathbf{r}_\perp}(\hat{n}_{j,\mathbf{r}_\perp}-1), \end{aligned} \tag{S.2}$$

with the dimensionless coupling strength $\alpha = K/\omega$. Going to momentum space, we find a time-dependent dispersion relation $\varepsilon_{\mathbf{q}}(t) = -2J\cos\left(q^x - \alpha\sin(\omega t+\varphi)\right) + \left(q^y\right)^2/(2m)$, oscillating at the driving frequency ω.

Simulating the out-of-equilibrium dynamics of the driven BHM is a challenging problem, for a multitude of reasons. The model being interacting, one cannot obtain a closed-form expression for its eigenstates and eigenenergies even in equilibrium, without using further approximations which come with their own applicability regimes. It is unfeasible to solve the time-dependent Schrödinger equation exactly, and one has to resort to numerical techniques. However, numerically simulating the dynamics of bosonic models is also difficult, due to the infinite dimensionality of the on-site Hilbert space. Additionally, many-body phenomena often require a large number of particles present in the system. State-of-the-art methods based on matrix product states, such as DMRG, are bound to area-law entanglement states, and are thus inapplicable to regimes, in which the 2D system heats up as a result of an external drive. While these issues represent only the tip of the iceberg, they already hint towards the necessity to develop various approximative methods to study the quantum evolution of interacting bosons.

The extraction of instability rates and unstable modes, presented in this paper, is based on the Bogoliubov approach, and we first derive it in this context [Secs. S2 A and S2 B]. We show how this leads to analytical predictions for the stability properties of the driven BHM [Sec. S2 C]. We then present two other alternative theoretical methods to tackle the driven BHM, namely the Weak Coupling Conserving Approximation (WCCA) [Sec. S2 D] and the Truncated Wigner Approximation (TWA) [Sec. S2 E] that are also discussed in the main text.

A. Time-Dependent Bogoliubov-de Gennes Equations

In the weakly-interacting regime, we base our analysis on Bogoliubov theory. Weakly-interacting bosons at ultracold temperatures form a Bose-Einstein condensate (BEC) which is macroscopically occupied, whereas the population of all other modes remains small compared to that of the condensate. This scale separation moti-

vates the Bogoliubov approximation:

$$\hat{a}_{\mathbf{q}_{BEC}} = \hat{b}_{\mathbf{q}_{BEC}} + \sqrt{N_{\rm BEC}(t)}, \qquad \hat{a}_{\mathbf{q}\neq\mathbf{q}_{BEC}} = \hat{b}_{\mathbf{q}\neq\mathbf{q}_{BEC}}, \tag{S.3}$$

where $N_{\rm BEC}(t)$ denotes the BEC population, $\mathbf{q}_{BEC}$ the mode in which condensation occurs, and $\hat{b}^\dagger_{\mathbf{q}}$ creates a particle of momentum $\mathbf{q}$ on top of the BEC background.

Plugging this ansatz into the Hamiltonian (S.1), and keeping terms to quadratic order in the operators $\hat{b}_{\mathbf{q}}$, we arrive at the time-dependent Bogoliubov Hamiltonian

$$H_{\rm B}(t) = \sum_{\mathbf{q}} (\varepsilon_{\mathbf{q}}(t) - \varepsilon_{\mathbf{q}_{BEC}}(t) + g)\hat{b}^\dagger_{\mathbf{q}}\hat{b}_{\mathbf{q}} + \frac{g}{2}\sum_{\mathbf{q}} \hat{b}^\dagger_{\mathbf{q}}\hat{b}^\dagger_{-\mathbf{q}} + \text{h.c.} \tag{S.4}$$

Here $g = Un$ and $n = N_{\rm BEC}(t=0)/V$ with $V = N^x_{\rm sites}\, N^\perp_{\rm sites}$, where $N^x_{\rm sites}$ and $N^\perp_{\rm sites}$ are the number of sites along the respective axis of the finite 2D system [see also Sec. S2 F]. Notice that the term $\varepsilon_{\mathbf{q}_{BEC}}(t)$ arises from the chemical potential which is here time-dependent, $\mu(t) = \varepsilon_{\mathbf{q}_{BEC}}(t) + g$, and which is fixed by the condition that the linear term (in $\hat{b}_{\mathbf{q}}, \hat{b}^\dagger_{\mathbf{q}}$) should vanish, to ensure the solution perturbs about a stable equilibrium point. The same result can be obtained from a linearization of the time-dependent Gross-Pitaevskii equation around the BEC wavefunction [S4, S5].

In the Bogoliubov approximation, the dynamics of the system is governed by the time-dependent Bogoliubov mode functions $u_{\mathbf{q}}(t)$ and $v_{\mathbf{q}}(t)$, defined through

$$\hat{b}_{\mathbf{q}}(t) = u_{\mathbf{q}}(t)\hat{\gamma}_{\mathbf{q}} + v^*_{-\mathbf{q}}(t)\hat{\gamma}^\dagger_{-\mathbf{q}}, \quad |u_{\mathbf{q}}(t)|^2 - |v_{\mathbf{q}}(t)|^2 = 1.$$

Using Heisenberg's equations of motion (EOM) $i\dot{\hat{b}}_{\mathbf{q}}(t) = [\hat{b}_{\mathbf{q}}(t), H_{\rm B}(t)]$, we arrive at the Bogoliubov-de Gennes (BdG) equations:

$$i\partial_t \begin{pmatrix} u_{\mathbf{q}} \\ v_{\mathbf{q}} \end{pmatrix} = \begin{pmatrix} \varepsilon_{\mathbf{q}}(t) - \varepsilon_{\mathbf{q}_{BEC}}(t) + g & g \\ -g & -\varepsilon_{-\mathbf{q}}(t) + \varepsilon_{\mathbf{q}_{BEC}}(t) - g \end{pmatrix} \begin{pmatrix} u_{\mathbf{q}} \\ v_{\mathbf{q}} \end{pmatrix}. \tag{S.5}$$

The Bogoliubov equations (S.5) describe the quasiparticle dynamics, and include the effects related to the micromotion, which were shown to play a crucial role in the stability of the system [S4].

B. Instability rate and most unstable mode

Due to the time-periodicity of Eq. (S.5), we base our stability analysis on Floquet theory, and focus thus on the stroboscopic propagator matrix $\Phi(T)$, which is obtained by time-evolving Eq. (S.5) over a single period T. The appearance of eigenvalues of $\Phi(T)$, $\epsilon_{\mathbf{q}}$, with positive imaginary parts indicates a dynamical instability, i.e. an exponential growth of the corresponding mode(s), characterized by the rate $s_{\mathbf{q}} = \text{Im}\ \epsilon_{\mathbf{q}}$. We then define the instability rate as the maximum growth rate:

$$\Gamma \equiv \max_{\mathbf{q}} s_{\mathbf{q}}. \tag{S.6}$$

It is independent of the reference frame (or gauge) and governs the stroboscopic dynamics of the mode functions $u_{\mathbf{q}}$ and $v_{\mathbf{q}}$ in the system (note that the number of exited atoms $n \sim \sum_{\mathbf{q}} |v_{\mathbf{q}}|^2$) has an instability rate 2Γ). We also introduce the most unstable mode

$$\mathbf{q}_{\rm mum} \equiv \underset{\mathbf{q}}{\text{argmax}}\ s_{\mathbf{q}}, \tag{S.7}$$

which is shown to provide clear experimental signatures of parametric instabilities (see main text).

C. Analytical treatment of parametric instabilities within the Bogoliubov approximation

We now recall the analytical method developed in Ref. [S5] to extract the instability properties of the system. The Bogoliubov equations of motion, Eq. (S.5), can be mapped to a parametric oscillator model [S6, S8], a seminal model of periodically-driven harmonic oscillator known to display parametric instabilities as soon as the drive frequency approaches twice the natural frequency. To see that, one should perform a series of suitable changes of basis and reference frames [S4] to recast the Bogoliubov equations into the form:

$$i\partial_t \begin{pmatrix} \tilde{u}'_{\mathbf{q}} \\ \tilde{v}'_{\mathbf{q}} \end{pmatrix} = \left[E^{\rm B}_{\rm eff}(\mathbf{q})\hat{\mathbf{1}} + \frac{A_{\mathbf{q}} E^{\rm B}_{\rm eff}(q)}{2} \begin{pmatrix} 0 & \cos(2\omega t)\mathrm{e}^{-2iE^{\rm B}_{\rm eff}(\mathbf{q})t} \\ -\cos(2\omega t)\mathrm{e}^{2iE^{\rm B}_{\rm eff}(\mathbf{q})t} & 0 \end{pmatrix} \right] \begin{pmatrix} \tilde{u}'_{\mathbf{q}} \\ \tilde{v}'_{\mathbf{q}} \end{pmatrix}, \tag{S.8}$$

where

$$E^{\rm B}_{\rm eff}(\mathbf{q}) = \sqrt{\left(4|J_{\rm eff}|\sin^2 q^x/2 + \left(\mathbf{q}^\perp\right)^2/2m\right)\left(4|J_{\rm eff}|\sin^2 q^x/2 + \left(\mathbf{q}^\perp\right)^2/2m + 2g\right)}, \tag{S.9}$$

denotes the effective (time-averaged) Bogoliubov dispersion, and where we introduced the amplitude

$$A_{\mathbf{q}} = 16J\mathcal{J}_2(K/\omega)\sin^2(q^x/2)\frac{g}{[E^{\mathrm{B}}_{\mathrm{eff}}(\mathbf{q})]^2}. \tag{S.10}$$

For the sake of simplicity, we have here restricted ourselves to the dominant harmonic of the drive, and dropped all terms in Eq. (S.8) that are irrelevant regarding the occurrence of instabilities – a simplification that was rigorously established in Ref. [S4]. As can be seen from a Rotating Wave Approximation treatment of Eq. (S.8), each momentum mode $\mathbf{q}$ will display a dynamical instability (characterized by an exponential growth of its population) whenever the drive frequency ω matches its effective Bogoliubov energy $E^{\mathrm{B}}_{\mathrm{eff}}(\mathbf{q})$, i.e. $\omega \approx E^{\mathrm{B}}_{\mathrm{eff}}(\mathbf{q})$. The parametric instability of a given mode is maximal at resonance ($\omega = E^{\mathrm{B}}_{\mathrm{eff}}(\mathbf{q})$), but still arises in a finite window around the resonance point. The associated instability rate is thus maximal at resonance, given by

$$\begin{aligned}\Gamma_{\mathbf{q}} &= A_{\mathbf{q}} E^{\mathrm{B}}_{\mathrm{eff}}(\mathbf{q}_{\mathrm{res}})/4 \\ &= 4Jg\mathcal{J}_2(K/\omega)\sin^2(q^x_{\mathrm{res}}/2)/E^{\mathrm{B}}_{\mathrm{eff}}(\mathbf{q}_{\mathrm{res}}).\end{aligned} \tag{S.11}$$

Close to resonance, it can be computed perturbatively using the detuning as the small parameter of the expansion: it is found to decrease with the distance from resonance, until vanishing at the edges of the instability domain [S6, S4].

From the knowledge of those individual rates, it is straightforward to infer the total instability rate Γ and the most unstable mode [see Eqs. (S.6) and (S.7)]. Here, those quantities are governed by resonant modes [i.e. fulfilling $\omega = E^{\mathrm{B}}_{\mathrm{eff}}(\mathbf{q})$], but a subtlety arises from the fact that there are generically multiple modes fulfilling this condition (corresponding to different q^x and $\mathbf{q}^\perp$), which do not have the same instability rate [see Eq. (S.11)]. To obtain the long-time instability rate Γ and the corresponding most unstable mode, one thus has to maximize Eq. (S.11) over all modes fulfilling the resonance condition $\omega = E^{\mathrm{B}}_{\mathrm{eff}}(\mathbf{q})$. Two regimes are obtained:

(I) If $\omega < \sqrt{4|J_{\mathrm{eff}}|(4|J_{\mathrm{eff}}| + 2g)}$, the most unstable mode corresponds to

$$q^x_{\mathrm{mum}} = 2\arcsin\sqrt{\frac{\sqrt{g^2+\omega^2}-g}{4|J_{\mathrm{eff}}|}}; \quad \mathbf{q}^\perp_{\mathrm{mum}} = 0. \tag{S.12}$$

In this case, the total instability rate is given by

$$\Gamma = (\sqrt{g^2+\omega^2} - g)\left|\frac{\mathcal{J}_2(K/\omega)}{\mathcal{J}_0(K/\omega)}\right|\frac{g}{\omega}. \tag{S.13}$$

(II) If $\omega > \sqrt{4|J_{\mathrm{eff}}|(4|J_{\mathrm{eff}}| + 2g)}$, which is often the case in the presence of transverse degrees of freedom (e.g. tubes or pancakes), the most unstable mode corresponds to

$$q^x_{\mathrm{mum}} = \pi; \quad (\mathbf{q}^\perp_{\mathrm{mum}})^2/2m = \sqrt{g^2+\omega^2} - g - 4|J_{\mathrm{eff}}|; \tag{S.14}$$

The total instability rate is given by the simple analytical formula

$$\Gamma = 4J\,|\mathcal{J}_2(K/\omega)|\,\frac{g}{\omega}. \tag{S.15}$$

D. Weak Coupling Conserving Approximation

The Bogoliubov approximation holds under the condition that the condensate occupation remains large throughout the duration of interest. A prerequisite for this is the presence of weak enough interaction strength $U/J \lesssim 1$, which renders the occurrence of quasiparticle collisions rare. Indeed, the Bogoliubov approximation holds when the latter do not play an important role, and thus can be neglected. This is the case, for instance, for weakly interacting bosons in equilibrium.

Away from equilibrium, however, excitations may form due to the drive, leading to fast depletion of the macroscopically occupied condensate, even though the interactions may still be small, compared to the bare hopping, at all times. The condensate depletion is enhanced when resonant transitions between the condensate mode and higher-energy states occur which, on the other hand, are stimulated by a periodic drive, as in the case of our study. Conceptually, one of the major drawbacks of the time-dependent Bogoliubov approximation is the lack of particle number conservation [S7]. This means that, even though it may capture the onset of condensate depletion, the approximation is doomed to fail in correctly predicting the dynamics of the quasiparticle distribution during the later stages of the evolution. One reason for this lies in the fact that the BdG EOM assume a constant in time, and thus endless, reservoir of particles provided by the macroscopically occupied condensate mode. One of the major results of our study is the identification and quantification of the time scales for the applicability of the time-dependent Bogoliubov approximation through a comparison with experiment.

An elegant way to restore particle number conservation is provided by the WCCA. It represents a minimal extension of the linearized Bogoliubov equations which conserves the corresponding global $U(1)$ symmetry at all times. The WCCA EOM is a set of coupled differential equations for the time-dependence of the condensate wavefunction $\phi(t)$ and the quasiparticle correlators F_{11} and F_{12}, defined as

$$\begin{aligned}\phi(t) &= \langle \hat{a}_{\mathbf{q}_{BEC}} \rangle, \\ F_{11}(t;\mathbf{q}) &= \frac{1}{2}\langle\{\hat{a}_{\mathbf{q}}(t), \hat{a}^\dagger_{\mathbf{q}}(t)\}\rangle_c = \frac{1}{2}\langle\{\hat{b}_{\mathbf{q}}(t), \hat{b}^\dagger_{\mathbf{q}}(t)\}\rangle, \\ F_{12}(t;\mathbf{q}) &= \langle\{\hat{a}_{\mathbf{q}}(t), \hat{a}_{-\mathbf{q}}(t)\}\rangle_c = \langle\{\hat{b}_{\mathbf{q}}(t), \hat{b}_{-\mathbf{q}}(t)\}\rangle,\end{aligned} \tag{S.16}$$

where, as before, $\hat{a}_{\mathbf{q}}$ describes the original bosonic degrees of freedom, while $\hat{b}_{\mathbf{q}}$ denotes the quasiparticle excitations [see Eq. (S.3)]. The subscript $_c$ denotes the connected correlation function $\langle AB\rangle_c = \langle AB\rangle - \langle A\rangle\langle B\rangle$ in the Bogoliubov ground state.

The WCCA equations can be derived by Legendre-transforming the action of the BHM on the Keldysh contour with respect to both the order parameter (condensate field) ϕ, and the quasiparticle propagators F_{11} and F_{12}. The resulting effective action, which contains all two-particle irreducible diagrams, is then expanded to leading order in the interaction strength U. Minimizing this effective action w.r.t. the condensate field and the propagators, one arrives at the following system of coupled integro-differential equations [S8]:

$$i\partial_t\phi(t) = [\varepsilon_{\mathbf{q}_{BEC}}(t) - \mu(t)]\phi(t) + \frac{U}{V}\left[[\phi(t)]^* [\phi(t)]^2 + 2\phi(t)\sum_{\mathbf{q}'} F_{11}(t;\mathbf{q}') + [\phi(t)]^* \sum_{\mathbf{q}'} F_{12}(t;\mathbf{q}')\right], \tag{S.17}$$

$$\partial_t F_{11}(t;\mathbf{q}) = 2\mathrm{Im}\left\{ \frac{U}{V}\left([\phi(t)]^2 + \sum_{\mathbf{q}'} F_{12}(t;\mathbf{q}')\right) [F_{12}(t;\mathbf{q})]^* \right\},$$

$$\begin{aligned} i\partial_t F_{12}(t;\mathbf{q}) = \{ &[\varepsilon_{\mathbf{q}}(t) + \varepsilon_{-\mathbf{q}}(t) - 2\mu(t)] F_{12}(t;\mathbf{q}) \\ &+ 2\frac{U}{V}\left[2\left(|\phi(t)|^2 + \sum_{\mathbf{q}'} F_{11}(t;\mathbf{q}')\right) F_{12}(t;\mathbf{q}) + \left([\phi(t)]^2 + \sum_{\mathbf{q}'} F_{12}(t;\mathbf{q}')\right) F_{11}(t;\mathbf{q})\right]\Big\}, \end{aligned}$$

where we denoted by * the complex conjugation. The initial condition is given by the Bogoliubov ground state, together with $|\phi(t=0)|^2 = N_{\mathrm{BEC}}(0)$. Notice that the presence of the chemical potential in the WCCA EOM is irrelevant to any observables, due to the $U(1)$-symmetry being conserved at all times, in contrast to the BdG EOM for which $\mu(t)$ is crucial to recover the correct spectrum of excitations. Hence, for the sake of a proper comparison between the different theoretical approximations, and without loss of generality, we may set $\mu(t) = \varepsilon_{\mathbf{q}_{BEC}}(t) + g$, which also fixes the reference frame.

One can convince oneself that, if one neglects all terms involving $\mathbf{q}'$-summations in Eqs. (S.17), the equation for the condensate wavefunction $\phi(t)$ decouples from the other two. Moreover, one may further recognize it as the Gross-Pitaevskii equation in the presence of the periodic drive. Using the definition (S.16), it follows that $F_{11}(t;\mathbf{q}) = 1/2(|u_{\mathbf{q}}(t)|^2 + |v_{\mathbf{q}}(t)|^2)$ and $F_{12}(t;\mathbf{q}) = u_{\mathbf{q}}(t)v_{\mathbf{q}}(t)$, and hence the remaining equations for F_{11} and F_{12} are equivalent to the BdG EOM from Eq. (S.5). Going back to the complete equations, we see that the $\mathbf{q}'$-summations represent the essential coupling between the condensate and the quasiparticle excitations, necessary to restore particle number conservation to leading order in U. The conserved quantity itself is the total number of condensed and excited atoms

$$\begin{aligned} N &= |\phi(t)|^2 + \sum_{\mathbf{q}} n_{\mathbf{q}}(t) \\ &= |\phi(t)|^2 + \sum_{\mathbf{q}}\left(F_{11}(t;\mathbf{q}) - \frac{1}{2}\right) = \text{const.} \end{aligned} \tag{S.18}$$

Despite the advantages of the WCCA EOM over the BdG equations mentioned above, let us make some important remarks about the applicability and usefulness of the WCCA. First, the WCCA EOM are not amenable to simple analytical treatment, due to their non-locality in momentum space. Second, unless condensate depletion is suppressed, e.g. by the existence of a pre-thermal phase [S8], the WCCA is also expected to be valid only in the short-time limit, since it misses the collisions between quasiparticles which appear first at order $\mathcal{O}(U^2)$. Thus, within the WCCA, a periodically driven system cannot thermalize which points out that the WCCA does not capture the later stages of the heating process. Going to order U^2 has been done recently in the large-N limit of the periodically-driven $O(N)$ model [S9, S10], and the existence of long-lived pre-thermal plateaus has been shown in the limit where the drive frequency is the largest energy scale in the problem.

E. Truncated Wigner Approximation

Since the exact quantum equations of motion for the BHM are often too hard to analyse, it may be advantageous to perform a semi-classical analysis. This proves particularly useful when the initial condition is deep into the superfluid phase, as the latter is well captured by the GPE, a classical nonlinear wave equation. Recently, it has been demonstrated that thermalization in classical Floquet systems behaves very similarly to their quantum counterparts [S11, S12, S13].

An elegant and systematic way of deriving the leading-order quantum corrections in the semiclassical limit, is to apply the TWA. The advantage of this method is that it is both particle-number conserving [since the GPE conserves $U(1)$ symmetry] and, at the same time, it is capable of capturing the thermalising dynamics induced by the periodic modulation at low driving frequencies [since the time-dependent GPE features chaotic dynamics]. Since there is extensive literature on the TWA al-

ready, below we only very briefly summarize the main ideas useful to our analysis, and refer the interested reader to Refs. [S14, S15] for a comprehensive review.

From translational invariance, it follows that the lowest-energy state of the BHM must necessarily be uniform in real space and, therefore, in momentum space the entire weight is carried by the $\mathbf{q}_{BEC} = 0$ mode. Thus, in the classical limit, the uniform condensate field obeys the following time-dependent GPE:

$$i\partial_t\phi(t) = (\varepsilon_{\mathbf{q}}(t) - \mu(t))\phi(t) + \frac{U}{V}|\phi(t)|^2\phi(t). \qquad \text{(S.19)}$$

Similar to the WCCA EOM, the presence of the chemical potential in the GPE is irrelevant to any observables, due to the $U(1)$-symmetry of the GPE. For instance $|\phi(t)|^2 = N_{\mathrm{BEC}} \approx N$ at all times.

In quantum mechanics, however, a small but finite fraction of atoms always occupies the excited modes of the system, even for weak interactions, known as quantum depletion. Let us again denote the Bogoliubov mode functions by $u_{\mathbf{q}}(t)$ and $v_{\mathbf{q}}(t)$, and recall that the complete atomic field expansion reads

$$\begin{aligned}\hat{a}_j &= \frac{1}{\sqrt{V}}\sum_{\mathbf{q}} \hat{a}_{\mathbf{q}} \mathrm{e}^{-i\mathbf{q}\cdot\mathbf{r}_j} = \sqrt{n}\hat{b}_{\mathbf{q}=0} + \frac{1}{\sqrt{V}}\sum_{\mathbf{q}\neq\mathbf{0}} \hat{b}_{\mathbf{q}}\mathrm{e}^{-i\mathbf{q}\cdot\mathbf{r}_j} \\ &= \sqrt{n}\hat{b}_{\mathbf{q}=0} + \frac{1}{\sqrt{V}}\sum_{\mathbf{q}\neq 0} u_{\mathbf{q}}\hat{\gamma}_{\mathbf{q}}\mathrm{e}^{-i\mathbf{q}\cdot\mathbf{r}_j} + v^*_{-\mathbf{q}}\hat{\gamma}^\dagger_{-\mathbf{q}}\mathrm{e}^{+i\mathbf{q}\cdot\mathbf{r}_j}.\end{aligned}$$

In the TWA [S14], the occupation of momentum mode $\mathbf{q}$ is described by a set of independent identically distributed complex-valued Gaussian random variables $\gamma_{\mathbf{q}}$, analogous to the quantum mechanical operators $\hat{\gamma}_{\mathbf{q}}$, such that the semiclassical condensate field is decomposed as

$$a_j = \sqrt{n} + \frac{1}{\sqrt{V}}\sum_{\mathbf{q}\neq 0} u_{\mathbf{q}}\gamma_{\mathbf{q}}\mathrm{e}^{-i\mathbf{q}\cdot\mathbf{r}_j} + v^*_{-\mathbf{q}}\gamma^*_{-\mathbf{q}}\mathrm{e}^{+i\mathbf{q}\cdot\mathbf{r}_j}. \qquad \text{(S.20)}$$

Since any Gaussian distribution is uniquely determined by its only two non-vanishing moments, we can choose the mean and variance of $\gamma_{\mathbf{q}}$ to correctly recover the true quantum mechanical fluctuations within the quadratic Bogoliubov theory [S14].

We can now use the TWA ansatz (S.20) as an initial condition for the GPE. Notice that this ansatz wavefunction is no longer uniform in space, due to the random contribution from the excited modes, and thus the time evolution needs to be computed in real space. Thus, within the TWA, the uniform condensate wavefunction is seeded with the correct quantum fluctuations, which ensures that the dynamics is captured correctly at the semiclassical level.

To compute expectation values of observables, we produce an ensemble of initial states a_j, time-evolve each state separately up to the time of interest, compute the observable for each realisation $a_j(t)$ separately, and perform an ensemble average in the very end. For example, the momentum distribution of the excitations within the TWA is given by

$$n_{\mathbf{q}\neq 0}(t) = \overline{\left|\frac{1}{\sqrt{V}}\sum_j a_j(t)\mathrm{e}^{i\mathbf{q}\cdot\mathbf{r}_j}\right|^2}, \qquad \text{(S.21)}$$

where $\overline{(\cdot)}$ stands for averaging over the random variable $\gamma_{\mathbf{q}}$.

While the TWA captures the effects of quasiparticle collisions to some extent, it should be noted that this formulation of quantum dynamics is not exact. One of the reasons for this is that we used Gaussian distributed random variables, whereas in general the true quantum distribution from the BHM has nonzero higher-order moments beyond the Bogoliubov approximation. While it is in principle possible to derive the next-to-leading-order correction within the TWA, due to its complexity, it is often beyond the scope of many theoretical studies.

F. Details of the Numerical Simulations for the homogeneous 2D system

While it is possible to simulate a 3D *homogeneous* system, the strong harmonic trap along the z-axis present in the experiment confines the system to a quasi-2D geometry. We therefore model the experiment by one lattice and one transverse degree of freedom. While the squeezed continuous z direction is irrelevant for the parametric instability effects within BdG theory, effects of the additional z-confinement are expected to be felt in the TWA simulations only at later times, beyond the regime of agreement between BdG and TWA (see Fig. 5 in the main text).

For the BdG and WCCA simulations, we use a condensate density of $n = 20$ to initialize the system in the Bogoliubov ground state. To determine the condensate wavefunction for the TWA, we use imaginary time evolution to find the lowest-energy state of the GPE in the presence of weak interactions, and consider an ensemble of 10^3 TWA realizations, performing an additional averaging over the phase of the drive φ to reduce the effects of the initial kick.

For all simulations, the momentum in the x direction (lattice) is discretized according to the quantization condition $q^x = 2\pi l/(N^x_{\mathrm{sites}}d)$ with $l \in [1, 2, \ldots, N^x_{\mathrm{sites}}]$. To simulate numerically the y (continuous) direction we apply the following auxiliary discretization: $q_\perp = 2\pi l_\perp/(N^\perp_{\mathrm{sites}}d_\perp)$ with $l_\perp \in [1, 2, \ldots, N^\perp_{\mathrm{sites}}]$, imposing an upper cutoff on the values of perpendicular momentum at $2\pi/d_\perp$. We checked that increasing this cutoff does not change the results, since high-momentum states have high energy and remain unaffected by the dynamics. Further, setting $N^x_{\mathrm{sites}} = 81$ and $N^\perp_{\mathrm{sites}} = 80$ modes, we find that the perpendicular momentum grid is dense enough for the system to be in the thermodynamic limit already at $d_\perp = d$. We further make sure the results remain unchanged with increasing the number of modes. Effects

due to the weak confining harmonic trap are not considered in these simulations, and are addressed separately as discussed in the main text. We use QuSpin [S16, S17] to simulate the dynamics.

G. Details of the Numerical Simulations for the inhomogeneous 1D system

The computational complexity of simulations in the presence of harmonic confinement limits the reachable system sizes. Unlike homogeneous systems, the inhomogeneity induced by the trap leads to a break-down of momentum conservation and couples all momentum modes. Hence, to determine the Bogoliubov mode functions, needed for the initial condition in all approximation methods discussed above, one has to exactly diagonalize a matrix of size $N_{\text{sites}} \times N_{\text{sites}}$, with N_{sites} the total number of space points. It is the size of this matrix, together with the additional bottlenecks for solving the corresponding equations of motion, which set the current limit on the reachable system sizes. For these reasons, simulating the dynamics of a 3D system in the thermodynamic limit ($N_{\text{sites}} \sim 10^6$) in the presence of a trap and subject to periodic modulation, is not feasible without introducing further approximations. We therefore limit the theoretical discussion of effects due to the harmonic trap to 1D lattices.

To obtain the numerical data in the presence of a harmonic trap potential, we simulate the BdG equations for a 1D lattice of $L_x/d = 201$ sites [S18]. We first performe imaginary time evolution in the presence of the trap to determine the exact initial condensate profile (main text Fig 3 inset). This inhomogeneous profile results in an inhomogeneous effective interaction strength $g(x)$, which is used to compute the Bogoliubov modes in the absence of the periodic drive used as an intial condition [S19]. Finally, the time-periodic BdG dynamics is simulated by solving the real-space variant of Eq. (S.5) with the additional replacement $g \to g(x)$.

H. Determining Interaction Parameter g in the Presence of a Weak Harmonic Trap

In the main text, we show that the presence of a weak harmonic trap is enough to render weakly-interacting bosonic periodically-driven systems unstable, even in the absence of transverse degrees of freedom. Fig. S3 (orange dots) shows the energy spectrum of the effective time-averaged Hamiltonian in the presence of the harmonic trap, and the corresponding drive-renormalized Bogoliubov dispersion (blue dots). Notice the presence of states above the Bogoliubov bandwidth (blue dashed line), which can get excited resonantly by the drive. In momentum space, these states occupy modes in the vicinity of $q^x = \pi$, and typically have weight over a finite range of momenta. Therefore, the presence of a weak harmonic

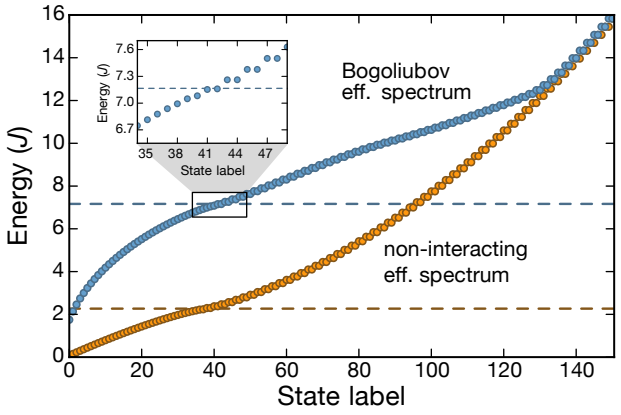

Figure S3. Energy spectrum of the non-interacting time-averaged Hamiltonian (orange dots) and corresponding effective Bogoliubov dispersion (blue dots) in a harmonic trap with $\omega_x = 0.26\ J/\hbar$. The dashed lines indicate the respective bandwidths in the homogenous case. Inset: As the energy reaches the homogenous bandwidth, the spectrum becomes quasidegenerate.

confinement causes the system to absorb energy even for $\omega > \omega_{\text{sat}}$, where unconfined systems are shown to be stable [S4].

The expressions for the saturation frequency ω_{sat} and the effective bandwidth W_{eff}, derived using translationally-invariant Bogoliubov theory, depend on the density-renormalized interaction parameter g. In the presence of a harmonic confinement, the condensate profile obeys Thomas-Fermi theory and is no longer uniform, which induces position dependence in $g \to g(x)$. At the same time, in the presence of the harmonic trap, there is no natural energy bandwidth to use. Hence, a natural question arises as to which value for g to use for the saturation frequency ω_{sat}, observed numerically in Fig. 6 in the main text. We find that the numerical simulations for the rates shown in Fig. 6 in the main text agree well with theory if we use the maximum value $g_{\max} = \max_x g(x)$. While we could not find a rigorous microscopic derivation of this observation due to the intractability of the inhomogeneous BdG equations, we do see a correlation between the energy at which the states in the Bogoliubov spectrum rapidly become quasidegenerate (Fig. S3 inset), and $\omega_{\text{sat}}(g_{\max}) = \sqrt{4J_{\text{eff}}(4J_{\text{eff}} + 2g_{\max})}$. This also coincides with the energy, starting from which the Bogoliubov states attain a significant occupation of the $q^x = \pi$ mode. It is very plausible that the same behavior carries over to higher dimensions. Therefore, in the presence of a harmonic trap, the maximum value $g_{\max}$ can be used to estimate the saturation frequency ω_{sat}.

S3. CONSTANTS

Variable	SI Units	Theory Units
d	425 nm	1 d
J	108 Hz$\times h$	1 J
E_R	7.1 kHz$\times h$	65.4 J
k_L	$739 \cdot 10^4$ $\frac{1}{\mathrm{m}}$	$\pi \frac{1}{d}$
$\hbar$	$1.05 \cdot 10^{-34}$ Js	1 $\hbar$
m	$6.5 \cdot 10^{-26}$ kg	0.07543 $\frac{\hbar^2}{Jd^2}$
U_0	$2.3 \cdot 10^{-51}$ Jm^3	0.4144 Jd^3
ζ	2.08	2.08
N	$3.7 \cdot 10^5$	3.7×10^5
ω_r	$2\pi\times$26 Hz	0.24 $\frac{J}{\hbar}$
ω_z	$2\pi\times$204 Hz	1.75 $\frac{J}{\hbar}$

[S1] B. Efron, J. Am. Stat. Assoc. **82**, 171 (1987).

[S2] L. Vidmar, J. P. Ronzheimer, M. Schreiber, S. Braun, S. S. Hodgman, S. Langer, F. Heidrich-Meisner, I. Bloch, and U. Schneider, Phys. Rev. Lett. **115**, 175301 (2015).

[S3] M. Reitter, J. Näger, K. Wintersperger, C. Sträter, I. Bloch, A. Eckardt, and U. Schneider, Phys. Rev. Lett. **119**, 200402 (2017).

[S4] S. Lellouch, M. Bukov, E. Demler, and N. Goldman, Phys. Rev. X **7**, 021015 (2017).

[S5] C. E. Creffield, Phys. Rev. A **79**, 063612 (2009).

[S6] L. D. Landau and E. M. Lifshitz, *Theoretical Physics - Vol. 1 Mechanics* (Pergamon Press, 1969).

[S7] This makes the dynamics sensitive to the value of the chemical potential used, which is counterintuitive, given that the starting point is the BHM where particle number is conserved.

[S8] M. Bukov, S. Gopalakrishnan, M. Knap, and E. Demler, Phys. Rev. Lett. **115**, 205301 (2015).

[S9] A. Chandran and S. L. Sondhi, Phys. Rev. B **93**, 174305 (2016).

[S10] S. A. Weidinger and M. Knap, Scientific Reports **7**, 45382 (2017).

[S11] O. Howell, P. Weinberg, D. Sels, A. Polkovnikov, and M. Bukov, arXiv **1802.04910** (2018).

[S12] S. Notarnicola, F. Iemini, D. Rossini, R. Fazio, A. Silva, and A. Russomanno, Phys. Rev. E **97**, 022202 (2018).

[S13] A. Rajak, R. Citro, and E. G. D. Torre, arXiv **1801.01142** (2018).

[S14] P. B. Blakie, A. S. Bradley, M. J. Davis, R. J. Ballagh, and C. W. Gardiner, Adv. Phys. **57**, 363 (2008).

[S15] A. Polkovnikov, Annals of Physics **325**, 1790 (2010).

[S16] P. Weinberg and M. Bukov, SciPost Phys. **2**, 003 (2017).

[S17] P. Weinberg and M. Bukov, arXiv **1804.06782** (2018).

[S18] Note that the momentum-space description is not useful here since the trap breaks momentum conservation.

[S19] D. A. W. Hutchinson, E. Zaremba, and A. Griffin, Phys. Rev. Lett. **78**, 1842 (1997).